Neurite beading is sufficient to decrease the apparent diffusion coefficient after ischemic stroke

Matthew D. Budde[a,1] and Joseph A. Frank[a,b]

[a]Radiology and Imaging Sciences, Clinical Center, and [b]Intramural Research Program, National Institute of Biomedical Imaging and Bioengineering, National Institutes of Health, Bethesda, MD 20892

Edited by Leslie G. Ungerleider, National Institute of Mental Health, Bethesda, MD, and approved July 6, 2010 (received for review April 9, 2010)

Diffusion-weighted MRI (DWI) is a sensitive and reliable marker of cerebral ischemia. Within minutes of an ischemic event in the brain, the microscopic motion of water molecules measured with DWI, termed the apparent diffusion coefficient (ADC), decreases within the infarcted region. However, although the change is related to cell swelling, the precise pathological mechanism remains elusive. We show that focal enlargement and constriction, or beading, in axons and dendrites are sufficient to substantially decrease ADC. We first derived a biophysical model of neurite beading, and we show that the beaded morphology allows a larger volume to be encompassed within an equivalent surface area and is, therefore, a consequence of osmotic imbalance after ischemia. The DWI experiment simulated within the model revealed that intracellular ADC decreased by 79% in beaded neurites compared with the unbeaded form. To validate the model experimentally, excised rat sciatic nerves were subjected to stretching, which induced beading but did not cause a bulk shift of water into the axon (i.e., swelling). Beading-induced changes in cell-membrane morphology were sufficient to significantly hinder water mobility and thereby decrease ADC, and the experimental measurements were in excellent agreement with the simulated values. This is a demonstration that neurite beading accurately captures the diffusion changes measured in vivo. The results significantly advance the specificity of DWI in ischemia and other acute neurological injuries and will greatly aid the development of treatment strategies to monitor and repair damaged brain in both clinical and experimental settings.

acute ischemia | diffusion-weighted MRI | cell swelling | Monte Carlo simulation

Diffusion-weighted MRI (DWI) is an exceptionally sensitive indicator of ischemic stroke and is, therefore, an important clinical diagnostic tool. Within minutes of the stroke onset, the microscopic motion of water molecules, termed the apparent diffusion coefficient (ADC), dramatically decreases in the infarcted brain region (1). However, the underlying cause of the decrease in ADC in still unknown. The available evidence suggests that the change is intimately related to cellular swelling (2, 3), but the precise biophysical mechanism remains elusive.

The CNS maintains a highly regulated ionic equilibrium, but oxygen and glucose deprivation, such as that experienced during ischemia, disrupts this delicate balance. In normally functioning neurons, the resting ionic balance across neuronal membranes is largely dependent on the transmembrane Na^+/K^+ ATPase, which removes intracellular Na^+ in exchange for the entry of K^+. The failure of this enzyme leads to an osmostic imbalance and swelling of the cell. It is believed that this rapid shift in water from the extracellular to the intracellular space causes ADC to decrease after ischemia, but exactly how this occurs is the subject of intense debate. Many theories have been proposed (4, 5), but none of these models has sufficiently captured both the magnitude of the measured diffusion changes and the underlying pathophysiology of injury. Unlike spherical cells that uniformly enlarge as they swell, axons and dendrites of the CNS, collectively known as neurites, undergo a shape transformation in response to swelling. Specifically, neurites exhibit focal enlargements separated by constrictions (6), or beading, in response to osmotic or ischemic conditions both in vivo and in vitro. Beading is governed by the biophysical properties of lipid membranes subjected to tension and hydrostatic pressure and has been described extensively in tubular membranes (7–9), stretched nerve fibers (10, 11), and neurons in vitro (12–14). Importantly, in vivo two-photon microscopy has revealed that beading occurs within minutes of an ischemic event in the brain and resolves on reperfusion (figure 5 in ref. 15), mirroring the temporal dynamics of ADC changes after ischemia. An investigation into the effects of neurite beading on the diffusion characteristics of CNS tissue has not been reported using a biophysically accurate model.

We propose that the undulation of the cell membrane induced by neurite beading is sufficient to decrease ADC after ischemia. In normal neurites, water mobility is highly restricted by the cell membrane perpendicular to the main axis, whereas water molecules diffusing along the main axis of the neurite encounter few barriers on the timescale of diffusion MRI measurements (16). Recently, it was shown in a model of global ischemia that diffusion within the intracellular space decreases to one-fourth of its preischemic value (17). Therefore, because cell membranes present the greatest hindrance to the diffusion of water molecules in biological tissues (18), we further hypothesize that the ADC decrease is specifically caused by a reduction in the mobility of intracellular water along the main axis of each neurite. First, we derive a model of beading in neurites that incorporates the known biophysics of cellular lipid membranes. Next, the DWI experiment was simulated in the geometrical beaded contours using a Monte Carlo random walk. Finally, the results were validated in excised rat sciatic nerves placed under tension, which induce axonal beading without causing a bulk shift in water between the intracellular and extracellular compartments. Taken together, the results shed light on the underlying mechanism that contributes to ADC decreases after an acute ischemic injury.

Results

A geometrical model of neurite beading was derived for increasing beading amplitudes under the constraints of conserved surface area and length (Fig. 1). The 2D contour was defined by the path traced by a point on an ellipse as it rolls along a fixed line. The 3D beaded cylinder, or unduloid, has a continuous and smooth surface, which mimics the properties of phospholipid membranes composing the neurite cell membrane. Compared with the original, unbeaded cylinder, the beaded morphology allows a greater volume to be contained within the equivalent surface area. Beading of the neurite membrane is, therefore, a consequence of ischemia-induced swelling. Thus, the proposed

Author contributions: M.D.B. designed research; M.D.B. performed research; M.D.B. analyzed data; and M.D.B. and J.A.F. wrote the paper.

The authors declare no conflict of interest.

This article is a PNAS Direct Submission.

[1]To whom correspondence should be addressed. E-mail: buddem@mail.nih.gov.

This article contains supporting information online at www.pnas.org/lookup/suppl/doi:10.1073/pnas.1004841107/-/DCSupplemental.

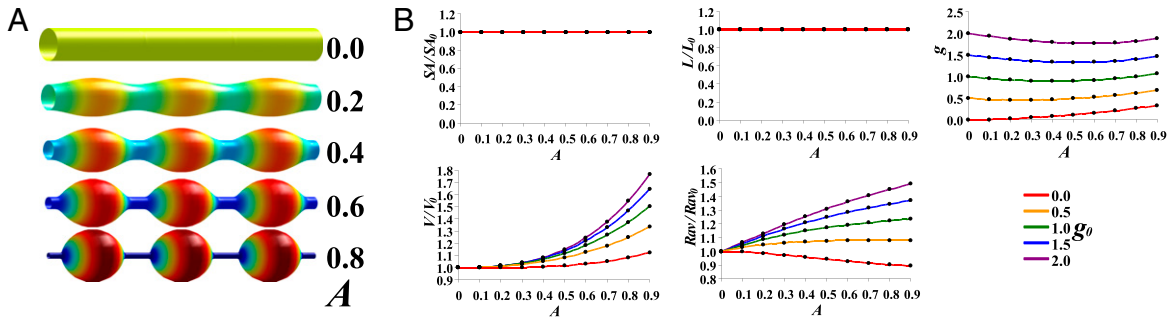

Fig. 1. Geometries and physical parameters of beading neurites. (*A*) The beaded cylinders are continuous, have smooth transitions between the enlargements and constrictions, and each of the displayed contours has identical surface area and length. (*B*) At all beading amplitudes, the surface area (SA) and length (L) were equivalent to the original cylinder of a given radius and bead separation. The resulting shape transformation yielded an increase in volume (V) as beading amplitude increased compared with the original cylinder. To meet the condition of conserved SA and L, the average radius (R_{av}) and bead separation (g) were varied as amplitude increased. Lines represent the analytical calculations of the physical parameters, and points indicate the equivalent parameters computed from the generated geometrical surfaces.

model accurately reflects the pathophysiology and biophysical properties of neurite beading after ischemia.

A Monte Carlo simulation of Brownian motion in the derived geometrical surfaces was performed, and the resulting DWI signal was estimated. The intracellular diffusion characteristics of the beaded cylinders were substantially altered by the changes in cell-membrane shape caused by beading (Fig. 2). Specifically, beading of the neurite membrane introduces barriers along the main axis of the neurite that limit water mobility along this axis. As a result, the intracellular diffusion parallel to the neurite ($ADC_{\parallel}$) substantially decreased with increasing beading amplitude, whereas only a minor change in diffusion perpendicular ($ADC_{\perp}$) was evident. Because intracellular $ADC_{\parallel}$ was orders of magnitude greater than $ADC_{\perp}$, the mean diffusivity [MD; MD = ($ADC_{\parallel}$ + 2*$ADC_{\perp}$)/3] mirrored the significant decrease in $ADC_{\parallel}$. In contrast, fractional anisotropy (FA) was decreased at only the largest beading amplitudes. The separation between beads (*g*) had only a negligible effect on the diffusion properties at the diffusion times used in the current study.

To examine the diffusion characteristics of the extracellular space, the geometrical contour was simplified to a sinusoidal expression, which allowed physiologically realistic volume fractions to be achieved without requiring the deformation of abutting contours (Fig. 3*A*). A hexagonal packing pattern of beading cylinders exhibits a local maximum volume fraction with amplitude of 0.73 in which the separation between the enlargements and constrictions is minimized. This volume fraction was set as the upper limit for all other beading amplitudes. The simplification of the geometrical contour had a negligible effect on the intracellular diffusion characteristics (Fig. 3*B*). Within the extracellular compartment, the increase in tortuosity because of beading caused a reduction in both $ADC_{\parallel}$ and $ADC_{\perp}$.

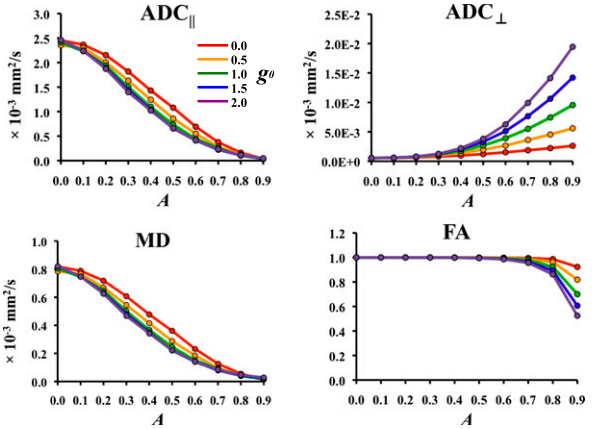

Fig. 2. Monte Carlo random-walk simulation of intracellular diffusion properties in beaded geometries. Intracellular diffusion was highly restricted parallel to the main axis ($ADC_{\parallel}$) with increasing beading amplitude. In contrast, diffusion perpendicular to the main axis ($ADC_{\perp}$) exhibited only a minimal increase and only at the largest beading amplitudes. MD was reduced with increasing beading amplitude, whereas FA was decreased at the largest amplitudes. The separation between beads (*g*) had only a marginal effect on the diffusion properties at the diffusion-weighting values used in the current study.

To validate the biophysical model in mammalian tissues, rat sciatic nerves were excised and subjected to stretching to induce beading (Fig. 4*A*). Stretching of the nerve imparts tension on the axonal cell membrane and causes it to bead in a manner consistent with the theoretical model. Therefore, in this system, the effects of the cell-membrane shape changes on diffusion properties can be measured without the confounding effects of a bulk water shift between the intracellular and extracellular compartments. $ADC_{\parallel}$ was significantly decreased ($P < 0.001$) in the beaded axons ($0.93 \pm 0.06 \times 10^{-3}$ mm^2/s) compared with unbeaded axons ($0.68 \pm 0.10 \times 10^{-3}$ mm^2/s) (Fig. 4*B*). $ADC_{\perp}$ was not statistically different between the beaded and unbeaded axons ($P = 0.25$). The significant decrease in MD ($P = 0.011$) was, therefore, caused by the hindrance of water mobility along the main axis of the axon. FA was unaffected ($P = 0.24$) despite the extensive beading. Beading also increased the non-Gaussian behavior of the diffusion-weighted signal as indicated by the increase in kurtosis parallel to the nerves but not perpendicular to them (Fig. S1). A second simulation was performed that replicated the ex vivo conditions using measurements derived from the microscopic images of sciatic nerves. Specifically, axons from control nerves ($n = 44$ axons in 3 nerves) had radii of 3.68 ± 1.86 (mean ± SD), whereas beaded axons from stretched nerves ($n = 50$ axons in 5 nerves) had radii of 2.87 ± 0.69 and beading amplitudes of 0.57 ± 0.15. The free diffusivity was set as the $ADC_{\parallel}$ measured ex vivo (0.925×10^{-3} mm^2/s), and diffusion-encoding parameters (Δ, δ, and G) were identical to those used ex vivo. The simulated diffusion properties (Fig. 4*C*) were in good agreement with the experimental values (Fig. 4*B*). $ADC_{\parallel}$ decreased by 26% and 31% in the measured and simulated conditions, respectively, compared with normal axons, whereas $ADC_{\perp}$ decreased by 15% and 10%, respectively. MD decreased by 23% and 25% in the nerves and simulated conditions, respectively, and FA decreased by 5% and 12% in the ex vivo and simulated conditions, respectively.

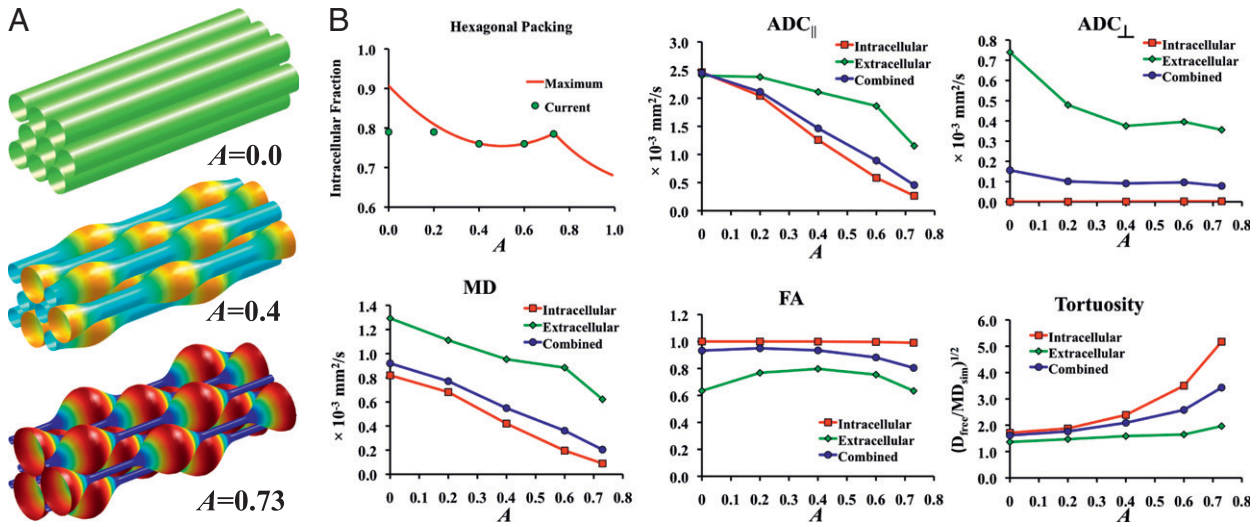

Fig. 3. Simulated diffusion properties of intra- and extracellular compartments in packed geometries of packed beading neurites. (*A*) Beading cylinders were packed in a hexagonal pattern. (*B*) The upper limit of the packing geometry was set at 0.79, and the local maximum was set at a beading amplitude of 0.73. Beading decreased $ADC_{\parallel}$ in both the intra- and extracellular compartments, whereas $ADC_{\perp}$ was substantially decreased only in the extracellular compartment. The decreases in MD were consequences of increased tortuosity occurring in both compartments.

Discussion

The predictions of the model are consistent with the changes in the diffusion properties of ischemic tissues in the mammalian brain measured in vivo using DWI. Osmolarity-induced beading in cultured neurons causes a beading amplitude of ~0.6, independent of the initial radius (19). In the current model, an amplitude of 0.6 and an initial radius of 1 μm resulted in an intracellular MD decrease of 79%. This agrees with the 76% decrease of intracellular MD measured in vivo after global ischemia (17), but it should be noted that there are significant limitations in the direct comparison between the two results. Specifically, the current model does not account for diffusion within cell bodies, axon terminals, and glial cells, including myelin, that could influence the measurements. Nonetheless, accounting for a neurite volume fraction of 60% measured in the normal rodent cortex (16, 20), the current model predicts a 47% decrease in MD, which is consistent with the 40–60% changes measured in vivo after ischemia (21). A decrease in extracellular water diffusivity has been shown to be similar to that of intracellular water after ischemia (22), and the current model predicts an extracellular diffusion decrease of 32% at a beading amplitude of 0.6. The corresponding tortuosity values and their changes because of beading are also consistent with those measured in vivo using a variety of compartment-specific tracers and

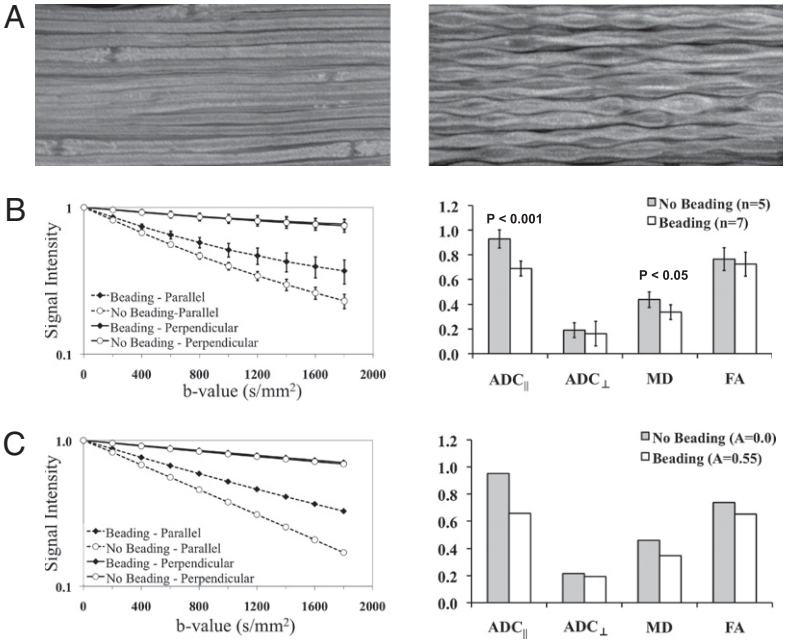

Fig. 4. Diffusion in excised, beaded sciatic nerve fibers. (*A*) Compared with the axons of control sciatic nerves, nerves fixed under tension display extensive beading of the axonal membrane. (*B*) Measurements of diffusion in the fixed nerves show a restriction of water mobility parallel to the axons but no change in the perpendicular direction. $ADC_{\parallel}$ was significantly decreased, whereas $ADC_{\perp}$ was unaffected. (*C*) Simulations performed with parameters and geometries mimicking the ex vivo situation were consistent with the ex vivo measurements.

methods (23). The tortuosity (λ) of the extracellular space exhibited an increase (0.29) because of beading similar to that measured in the ischemic rat cortex (24). Conversely, the intracellular tortuosity exhibited a considerably greater increase (1.65). It should be noted that because of the constraints associated with tightly packing the 3D beaded geometries, the volume fractions were nearly identical throughout the range of beading amplitudes. Therefore, the changes in the extracellular diffusivity were caused solely by changes in morphology, although the extracellular fraction is known to decrease (24). Nonetheless, the current model shows that a 5–10% shift of bulk water from the extracellular to the intracellular compartment (13, 24) would be sufficient to induce neurite beading, causing a substantial decrease in intracellular MD and thereby decreasing overall MD by nearly one-half. Unlike previous models that depict axonal swelling as balloon-like expansion (25, 26), the conservation of surface area more realistically mimics the biophysical properties of neurite swelling. These properties are intrinsic to cylindrical cell membranes and resolve the contradictory observations in spherical cells that swelling increases intracellular ADC (27, 28).

In addition to the directionally independent MD, the diffusion properties parallel and perpendicular to the white-matter fibers exhibit important differences. In white matter in the human (29) and rodent (30) brain, both $ADC_{\parallel}$ and $ADC_{\perp}$ have similar fractional decreases. The current model shows a similar, although not identical, fractional decrease in $ADC_{\parallel}$ and $ADC_{\perp}$ of 64% and 38%, respectively. Whereas the decrease in $ADC_{\parallel}$ is largely dominated by intracellular diffusivity, $ADC_{\perp}$ is modulated by the extracellular diffusivity (4). Thus, the packing geometry and volume fractions influence $ADC_{\perp}$ to a much greater degree. Because of the similar fractional decreases of both $ADC_{\parallel}$ and $ADC_{\perp}$, a change in white-matter anisotropy was generally not observed in ischemia, although reports have been conflicting (31, 32). Our simulation results depict only a small decrease in FA at only the largest beading amplitudes, and FA was not significantly reduced in the stretched sciatic nerve. The current work examined and simulated ADC changes in coherently arranged fibers, but the model can similarly be extrapolated to the randomly oriented network of dendrites and axons composing gray matter. Diffusion in gray matter is nearly isotropic, and $ADC_{\parallel}$ and $ADC_{\perp}$ cannot be reliably distinguished. However, the $ADC_{\parallel}$ within individual neurites should decrease, regardless of their orientation, and the locally reduced $ADC_{\parallel}$ contributes to the overall decrease of MD. Correspondingly, recent work has shown that $ADC_{\parallel}$ in white matter is specific for acute axonal injury in animal models of spinal cord injury (33), multiple sclerosis (34), traumatic brain injury (35), and others. It is of considerable interest whether the diffusion changes observed in these and other acute injuries can be attributed to cell-membrane changes similar to those described in this work.

The beading of neurites in response to the metabolic and osmotic changes after ischemia has been extensively shown in vitro, ex vivo, and in vivo. Cultured dorsal-root axons bead within 1 min after hyposmotic changes to the bathing medium (13). In contrast, acute brain preparations have shown that dendrites do not exhibit beading after osmotic challenge, but they do so quite rapidly after oxygen-glucose deprivation (37). In vivo, visualization of dendritic beading using two-photon microscopy shows that beading occurs within minutes of an ischemic event, resolves quickly after reperfusion (15), and extends beyond the ischemic core of the lesion (6). Similar characteristics are evident in ADC measurements in vivo (38). Unlike neurons, however, astrocytes do not appear to exhibit beading in response to either osmotic or oxygen-glucose perturbations (39), despite their extensive arborizations. The difference is likely related to the high expression of aquaporins on astrocytes, whereas neurons lack such water channels (37). Additionally, dendritic beading has been observed in vivo in animals models of cortical spreading depression (40) and epilepsy (41) after focal KCl and systemic kainate administration, respectively, as well as excitotoxic events in vitro (42). ADC is also significantly reduced in these models (43, 44). Although beading occurs within minutes after acute ischemia, injured axons and dendrites eventually undergo Wallerian degeneration. This degenerative process may cause the subsequent normalization and increased MD in the days and weeks after the initial insult. Therefore, attributing diffusion changes to beading may likely be only valid for acute neurological injuries.

The proposed model does have other assumptions and limitations that must be considered. Cell membranes impart the greatest restriction to water mobility in biological tissues (18). However, membrane permeability can influence the observed diffusion measurements (26), and this contribution becomes increasingly important with longer diffusion-encoding times (Δ) used in human studies. Our simulations used a single and relatively short diffusion-encoding time (18 ms). Further simulations and experimental studies that incorporate permeability changes with greater diffusion weightings may elucidate more complex features of the beading morphology. We also purposely neglected other structures composing CNS tissues, including neuronal cell bodies, glial cells, and subcellular organelles and cytoskeletal elements that contribute in unique ways to the diffusion properties of normal and injured tissues. Nonetheless, compared with models that implicate changes in bulk-water compartmentalization or extracellular tortuosity for the decrease in MD, the finding that these changes are dominated by intracellular diffusion is largely supported by experimental studies (17, 45). Similarly, the beading model of decreased intracellular diffusion is well-suited to validation using MR-based or microscopy-based techniques.

Conclusions

We have shown that neurite beading is sufficient to account for the ADC decrease after acute ischemia by restricting intracellular water mobility along the length of the neurite. This model includes a biophysically accurate model of neurite swelling that sufficiently captures the diffusion changes measured in vivo as well as the known pathology of ischemic injury.

Materials and Methods

Theory. ***Analytical model of beaded cylinders.*** The contour of a beaded cylinder is composed of alternating enlargements and constrictions defined by the average radius (R_{av}) and dimensionless beading amplitude (A). The contour of beading was elucidated in nerve fibers subjected to stretch (10) as (Eq. **1**)

$$x(R) = x(R_{\min}) + R_{av}\int_{1-A}^{R/R_{av}} f(\varepsilon)d\varepsilon, \qquad [1]$$

where (Eq. **2**)

$$f(\varepsilon) = \frac{\left(\varepsilon^2 + 1 - A^2\right)}{\sqrt{4\varepsilon^2 - \left(\varepsilon^2 + 1 - A^2\right)^2}} \qquad [2]$$

The length (L), surface area (SA), and volume (V) of a single bead were, therefore, revealed to be (Eqs. **3** and **4**)

$$L_B = 2R_{av}\int_{1-A}^{1+A} f(\varepsilon)d\varepsilon, \qquad [3]$$

$$SA_B = 4\pi R_{av}^2\int_{1-A}^{1+A} \varepsilon\sqrt{1 + f^2(\varepsilon)}d\varepsilon, \qquad [4]$$

and (Eq. **5**)

$$V_B = 2\pi R_{av}^3 \int_{1-A}^{1+A} \varepsilon^2 f(\varepsilon) d\varepsilon, \quad [5]$$

respectively. Although beads can be located adjacent to one another, they can also be separated by a compacted neck of uniform radius R_{min} with a length proportional to the initial radius (R_i) of the unbeaded cylinder, $g = \frac{L_C}{2\pi R_i}$. Including the compacted neck into Eqs. **3**–**5** yields (Eqs. **6**–**8**).

$$L_{tot} = 2R_{av} \int_{1-A}^{1+A} f(\varepsilon) d\varepsilon + 2\pi R_{av} g \quad [6]$$

$$SA_{tot} = 4\pi R_{av}^2 \int_{1-A}^{1+A} \varepsilon \sqrt{1 + f^2(\varepsilon)} d\varepsilon + 4\pi R_{av}(1-A) \cdot \pi R_{av} g \quad [7]$$

$$V_{tot} = 2\pi R_{av}^3 \int_{1-A}^{1+A} \varepsilon^2 f(\varepsilon) d\varepsilon + 2\pi R_{av}^2 (1-A)^2 \cdot \pi R_{av} g \quad [8]$$

It is assumed that beading induced by osmotic changes resulting from ischemia does not significantly change the length and surface area of each neurite compared with the cylinder from which it originated. To meet this condition, the two equations $L_A - L_0 = 0$ and $SA_A - SA_0 = 0$ must be satisfied. Substituting Eqs. **6** and **7** results in a system of two equations (Eqs. **9** and **10**):

$$\left(R_{av}^2 \int_{1-A}^{1+A} \varepsilon \sqrt{1 + f^2(\varepsilon)} d\varepsilon + (1-A) R_{av} \cdot \pi R_i g \right) - \left(\pi R_i^2 + \pi R_i^2 g_0 \right) = 0 \quad [9]$$

$$\frac{\left(\pi R_i + \pi R_i g_0 - R_{av} \int_{1-A}^{1+A} f(\varepsilon) d\varepsilon \right)}{\pi R_{av}} - g = 0 \quad [10]$$

where the initial radius (R_i), bead separation (g_0), and beading amplitude (A) are constants and the final average radius (R_{av}) and final bead separation (g) are free parameters. For each A, there exists a single positive solution for R_{av} and g that satisfies the condition of conserved length and surface area while preserving the shape of the beaded contour.

Geometrical model of beaded cylinders. The equivalent Cartesian coordinates for the contour of a beaded cylinder are derived from the geometrical path traced by a point on an ellipse as it rolls along an axis (46) (Eqs. **11** and **12**):

$$x_i = \int_0^{\theta} \sqrt{a^2 \sin^2\phi + b^2 \cos^2\phi} d\phi + \frac{\left(a + \sqrt{a^2 - b^2} \cos\theta \right) \cdot \sqrt{a^2 - b^2} \sin\theta}{\sqrt{a^2 \sin^2\theta + b^2 \cos^2\theta}} \quad [11]$$

$$y_i = \frac{b\left(a + \sqrt{a^2 - b^2} \cdot \cos\theta \right)}{\sqrt{a^2 \sin^2\theta + b^2 \cos^2\theta}} \quad [12]$$

where $a = R_{av}$, $b = \sqrt{R_{av}^2(1 - A^2)}$ and θ is the angle of rotation. A single beaded contour is formed for $\theta = [-\pi, \pi]$, yielding a straight line when A = 0 and a semicircle when A = 1. The separation between the beads is composed of a cylinder of radius R_{min} and length g. The 2D curve rotated about the x axis depicts the full axisymmetric 3D mesh model, the shape of which was first referred to as an unduloid (47). The physical properties of the geometrical 3D surfaces, including surface area, volume, and length, were computed using numerical integration for axisymmetric contours (Eq. **13**–**15**):

$$SA = \sum_{i=1}^{n-1} \pi (y_i + y_{i+1}) \sqrt{(y_i - y_{i+1})^2 + (x_i - x_{i+1})^2} \quad [13]$$

$$V = \sum_{i=1}^{n-1} \frac{\pi}{3} (x_i + x_{i+1}) \left(y_i^2 + y_i y_{i+1} + y_{i+1}^2 \right) \quad [14]$$

$$L = x_n - x_1 \quad [15]$$

where x and y are the points of the 2D contour from Eqs. **11** and **12** and n is the number of points of the surface.

Extracellular space and packed geometries. To examine the contribution of the extracellular space, cylinders were arranged in a hexagonal pattern. To achieve a specified volume fraction without allowing overlap or deformation of adjacent geometries, the beaded contour was simplified to a sinusoidal expression by substituting $x_i = R_{av} \cdot \theta$ and $y_i = R_{av}(A \cdot \cos(\theta) + 1)$ for Eqs. **11** and **12**, respectively. For beaded cylinders packed in a hexagonal pattern, a local maximum volume fraction of 0.79 occurs at $A = \sqrt{3} - 1$. The separation between cylinders was scaled to constrain the maximum volume fraction to this value for all beading amplitudes.

Methods. ***Geometrical model.*** Mesh geometries were created for an initial radius (R_i) of 1 μm at amplitudes (A) of 0.0–0.9 in steps of 0.1 and initial bead separations (g_0) of 0.0–2.0 in steps of 0.5. The selected step size of θ resulted in 625 polygon faces for unit volume, which consisted of a single bead and one-half of the constriction at each end. The system of Eqs. **9** and **10** was solved using the optimization toolbox of Matlab (Mathworks) and was used in the construction of the mesh geometries. Packed geometries used a separation (g) of 0.5 to maximize packing density.

Simulation. Diffusion measurements were simulated using a Monte Carlo random walk implemented in the Camino diffusion toolkit (25). Spins were initially positioned randomly in the either the intracellular or extracellular space in the center unit volume and were contained within their respective compartments throughout the simulation. The membrane was impermeable, and spins encountering the boundary were elastically reflected. The unit volume was repeated along the primary axis to ensure that spins did not escape the ends of the geometry. The free diffusion constant was 80% of that of free water (2.4×10^{-3} mm^2/s) (48); 10,000 spins were simulated in 400 time steps. Spin phase was updated at each time step during the diffusion encoding, and signal intensity was calculated as the phase-sensitive average of all spins. The effects of T2 decay were omitted. The diffusion encoding used a diffusion time (δ) of 18 ms, a diffusion gradient-encoding duration (Δ) of 6 ms, and a gradient strength (G) of 15 G/cm to yield a b value of 1,000 s/mm^2. Diffusion encoding was measured along the three orthogonal axes, and the diffusivities were computed for each direction using the equation $S_i = S_0 \exp(-bD)$. Diffusion parameters were summarized as diffusion coefficients parallel ($ADC_{\parallel}$) and perpendicular ($ADC_{\perp}$) to the geometry, the rotationally invariant MD [MD = ($ADC_{\parallel}$ + $ADC_{\perp}$ × 2)/3], and the fractional anisotropy. A separate simulation was performed to mimic the ex vivo sciatic nerve experiment described below that used identical diffusion weighting, geometrical parameters derived from microscopic images, and a free diffusivity as the measured $ADC_{\parallel}$ value.

Sciatic nerve preparation. Six 6- to 10-wk-old Wistar rats were euthanized using an overdose of pentobarbital. The right and left sciatic nerves were excised and maintained in cold Ringer's solution. Using a dissection microscope, excess tissue was removed, the perineural sheath was slit lengthwise (49), and nerves were ligated at each end and fastened to screws mounted on a plastic support. Each nerve was subjected to stretching in one of two conditions. Five nerves underwent a slight stretch (<1 g) until the bands of Fontana were hardly visible under incident light (50), which serves to straighten the axonal fibers but does not induce beading. The remaining seven nerves underwent a severe stretch (>20 g) until the bands of Fontana had completely disappeared, which causes beading of the axonal cell membrane. Within 30 s of stretching, nerves remained stretched, were immersed in 0 °C 2% glutaraldehyde and 2% paraformaldehyde solution in PBS, and remained in fixative overnight. The perineural sheath was completely dissected away from the nerve fibers the next day.

Ex vivo diffusion MRI. Extraneural water on the external surfaces of the fixed nerves was removed using an absorbent tissue, and nerves were immersed in a 10-cm glass NMR tube containing a proton-free fluid (Fomblin) to prevent further drying. The preparation was placed in a 10-cm inner diameter birdcage coil and inserted into a 7-T vertical-bore magnet (Bruker BioSpin). Scout images were acquired to properly align the slice direction orthogonal to the primary nerve axis. A pulsed gradient spin-echo sequence [repetition time (TR) = 5,000 ms and echo time (TE) = 30 ms] was used with three orthogonal diffusion-weighting directions. For each direction, 9 b values from 0 to 1,800 s/mm^2 were incremented in steps of 200, with a diffusion gradient

duration (δ) of 4 ms and a separation (Δ) of 15 ms. A slice-selective excitation and refocusing pulse with a thickness of 9 mm was oriented perpendicular to the nerve to avoid effects from the cut ends of the nerve. ADC values for each diffusion direction were derived by a least-squares fit of the diffusion-weighted signal intensity to a single exponential function using b values 0 through 1,000. Summary parameters $ADC_{\parallel}$, $ADC_{\perp}$, MD, and FA were computed as described.

Confocal microscopy. Nerves were whole-mounted on glass slides. A laser scanning confocal microscope (Zeiss) was used to acquire z stack images at ×20 magnification using an excitation wavelength of 546 nm, highlighting the autofluorescence of aldehyde-fixed myelin (51). Maximum intensity projections over a 30-μm section were created. The mean radius was measured from control nerves (n = 3), and the beading amplitude [$A = (R_{max} - R_{min})/(R_{max} + R_{min})$] and average radius [$R_{av} = (R_{max} + R_{min})/2$] were measured from stretched nerves (n = 5).

Statistical analysis. A Student t test was used to compare the diffusion summary parameters between the beaded and unbeaded conditions at a significance threshold of $P < 0.05$.

ACKNOWLEDGMENTS. We thank the Biomedical Magnetic Resonance Laboratory at Washington University in St. Louis, MO, for use of their computational resources supported in part by National Institutes of Health Grant U24-CA83060 (J.J.H. Ackerman, PI) and Dr. Matt Hall for assistance with the Camino software. This work was supported by the Intramural Research Program of Clinical Center at the National Institutes of Health and an National Institutes of Health Predoctoral National Research Service Award fellowship (to M.D.B).

1. Moseley ME, et al. (1990) Diffusion-weighted MR imaging of acute stroke: Correlation with T2-weighted and magnetic susceptibility-enhanced MR imaging in cats. *AJNR Am J Neuroradiol* 11:423–429.
2. Norris DG (2001) The effects of microscopic tissue parameters on the diffusion weighted magnetic resonance imaging experiment. *NMR Biomed* 14:77–93.
3. Sotak CH (2004) Nuclear magnetic resonance (NMR) measurement of the apparent diffusion coefficient (ADC) of tissue water and its relationship to cell volume changes in pathological states. *Neurochem Int* 45:569–582.
4. Ford JC, Hackney DB (1997) Numerical model for calculation of apparent diffusion coefficients (ADC) in permeable cylinders—comparison with measured ADC in spinal cord white matter. *Magn Reson Med* 37:387–394.
5. Szafer A, Zhong J, Gore JC (1995) Theoretical model for water diffusion in tissues. *Magn Reson Med* 33:697–712.
6. Murphy TH, Li P, Betts K, Liu R (2008) Two-photon imaging of stroke onset in vivo reveals that NMDA-receptor independent ischemic depolarization is the major cause of rapid reversible damage to dendrites and spines. *J Neurosci* 28:1756–1772.
7. Bar-Ziv R, Moses E (1994) Instability and "pearling" states produced in tubular membranes by competition of curvature and tension. *Phys Rev Lett* 73:1392–1395.
8. Bar-Ziv R, Moses E, Nelson P (1998) Dynamic excitations in membranes induced by optical tweezers. *Biophys J* 75:294–320.
9. Shemesh T, Luini A, Malhotra V, Burger KN, Kozlov MM (2003) Prefission constriction of Golgi tubular carriers driven by local lipid metabolism: A theoretical model. *Biophys J* 85:3813–3827.
10. Markin VS, Tanelian DL, Jersild RA, Jr, Ochs S (1999) Biomechanics of stretch-induced beading. *Biophys J* 76:2852–2860.
11. Ochs S, Pourmand R, Jersild RA, Jr, Friedman RN (1997) The origin and nature of beading: A reversible transformation of the shape of nerve fibers. *Prog Neurobiol* 52: 391–426.
12. Nakayama Y, Aoki Y, Niitsu H (2001) Studies on the mechanisms responsible for the formation of focal swellings on neuronal processes using a novel in vitro model of axonal injury. *J Neurotrauma* 18:545–554.
13. Pullarkat PA, Dommersnes P, Fernández P, Joanny JF, Ott A (2006) Osmotically driven shape transformations in axons. *Phys Rev Lett* 96:048104.
14. Roediger B, Armati PJ (2003) Oxidative stress induces axonal beading in cultured human brain tissue. *Neurobiol Dis* 13:222–229.
15. Li P, Murphy TH (2008) Two-photon imaging during prolonged middle cerebral artery occlusion in mice reveals recovery of dendritic structure after reperfusion. *J Neurosci* 28:11970–11979.
16. Jespersen SN, Kroenke CD, Østergaard L, Ackerman JJ, Yablonskiy DA (2007) Modeling dendrite density from magnetic resonance diffusion measurements. *Neuroimage* 34: 1473–1486.
17. Goodman JA, Ackerman JJ, Neil JJ (2008) Cs + ADC in rat brain decreases markedly at death. *Magn Reson Med* 59:65–72.
18. Beaulieu C (2002) The basis of anisotropic water diffusion in the nervous system—a technical review. *NMR Biomed* 15:435–455.
19. Tanelian DL, Markin VS (1997) Biophysical and functional consequences of receptor-mediated nerve fiber transformation. *Biophys J* 72:1092–1108.
20. Chklovskii DB, Schikorski T, Stevens CF (2002) Wiring optimization in cortical circuits. *Neuron* 34:341–347.
21. Liu KF, et al. (2001) Regional variations in the apparent diffusion coefficient and the intracellular distribution of water in rat brain during acute focal ischemia. *Stroke* 32: 1897–1905.
22. Duong TQ, et al. (2001) Extracellular apparent diffusion in rat brain. *Magn Reson Med* 45:801–810.
23. Duong TQ, Ackerman JJ, Ying HS, Neil JJ (1998) Evaluation of extra- and intracellular apparent diffusion in normal and globally ischemic rat brain via ^{19}F NMR. *Magn Reson Med* 40:1–13.
24. Homola A, Zoremba N, Slais K, Kuhlen R, Syková E (2006) Changes in diffusion parameters, energy-related metabolites and glutamate in the rat cortex after transient hypoxia/ischemia. *Neurosci Lett* 404:137–142.
25. Hall M, Alexander D (2009) Convergence and parameter choice for Monte-Carlo simulations of diffusion MRI. *IEEE Trans Med Imaging* 28:1354–1364.
26. Landman BA, et al. (2010) Complex geometric models of diffusion and relaxation in healthy and damaged white matter. *NMR Biomed* 23:152–162.
27. Trouard TP, Harkins KD, Divijak JL, Gillies RJ, Galons JP (2008) Ischemia-induced changes of intracellular water diffusion in rat glioma cell cultures. *Magn Reson Med* 60:258–264.
28. Sehy JV, Ackerman JJ, Neil JJ (2002) Evidence that both fast and slow water ADC components arise from intracellular space. *Magn Reson Med* 48:765–770.
29. Sorensen AG, et al. (1999) Human acute cerebral ischemia: Detection of changes in water diffusion anisotropy by using MR imaging. *Radiology* 212:785–792.
30. Sun SW, et al. (2005) Formalin fixation alters water diffusion coefficient magnitude but not anisotropy in infarcted brain. *Magn Reson Med* 53:1447–1451.
31. van Gelderen P, et al. (1994) Water diffusion and acute stroke. *Magn Reson Med* 31: 154–163.
32. Sotak CH (2002) The role of diffusion tensor imaging in the evaluation of ischemic brain injury—a review. *NMR Biomed* 15:561–569.
33. Loy DN, et al. (2007) Diffusion tensor imaging predicts hyperacute spinal cord injury severity. *J Neurotrauma* 24:979–990.
34. Budde MD, et al. (2008) Axonal injury detected by in vivo diffusion tensor imaging correlates with neurological disability in a mouse model of multiple sclerosis. *NMR Biomed* 21:589–597.
35. Mac Donald CL, Dikranian K, Bayly P, Holtzman D, Brody D (2007) Diffusion tensor imaging reliably detects experimental traumatic axonal injury and indicates approximate time of injury. *J Neurosci* 27:11869–11876.
36. Kerschensteiner M, Schwab ME, Lichtman JW, Misgeld T (2005) In vivo imaging of axonal degeneration and regeneration in the injured spinal cord. *Nat Med* 11: 572–577.
37. Andrew RD, Labron MW, Boehnke SE, Carnduff L, Kirov SA (2007) Physiological evidence that pyramidal neurons lack functional water channels. *Cereb Cortex* 17: 787–802.
38. Li F, et al. (2002) Acute postischemic renormalization of the apparent diffusion coefficient of water is not associated with reversal of astrocytic swelling and neuronal shrinkage in rats. *AJNR Am J Neuroradiol* 23:180–188.
39. Risher WC, Andrew RD, Kirov SA (2009) Real-time passive volume responses of astrocytes to acute osmotic and ischemic stress in cortical slices and in vivo revealed by two-photon microscopy. *Glia* 57:207–221.
40. Takano T, et al. (2007) Cortical spreading depression causes and coincides with tissue hypoxia. *Nat Neurosci* 10:754–762.
41. Zeng LH, et al. (2007) Kainate seizures cause acute dendritic injury and actin depolymerization in vivo. *J Neurosci* 27:11604–11613.
42. Hasbani MJ, Schlief ML, Fisher DA, Goldberg MP (2001) Dendritic spines lost during glutamate receptor activation reemerge at original sites of synaptic contact. *J Neurosci* 21:2393–2403.
43. de Crespigny A, Röther J, van Bruggen N, Beaulieu C, Moseley ME (1998) Magnetic resonance imaging assessment of cerebral hemodynamics during spreading depression in rats. *J Cereb Blood Flow Metab* 18:1008–1017.
44. Latour LL, Hasegawa Y, Formato JE, Fisher M, Sotak CH (1994) Spreading waves of decreased diffusion coefficient after cortical stimulation in the rat brain. *Magn Reson Med* 32:189–198.
45. Silva MD, et al. (2002) Separating changes in the intra- and extracellular water apparent diffusion coefficient following focal cerebral ischemia in the rat brain. *Magn Reson Med* 48:826–837.
46. Toyama K (2004) Self-parallel constant mean curvature surfaces. *Electronic Geometry Models*. Available at http://www.eg-models.de/. Accessed January 10, 2009.
47. Delaunay C (1841) Sur la surface de revolution dont la courbure moyenne est constante. *J Math Pures Appl* 6:309–315.
48. Beaulieu C, Allen PS (1994) Water diffusion in the giant axon of the squid: Implications for diffusion-weighted MRI of the nervous system. *Magn Reson Med* 32: 579–583.
49. Ochs S, Jersild RA, Jr, Pourmand R, Potter CG (1994) The beaded form of myelinated nerve fibers. *Neuroscience* 61:361–372.
50. Pourmand R, Ochs S, Jersild RA, Jr (1994) The relation of the beading of myelinated nerve fibers to the bands of Fontana. *Neuroscience* 61:373–380.
51. Reynolds RJ, Little GJ, Lin M, Heath JW (1994) Imaging myelinated nerve fibres by confocal fluorescence microscopy: individual fibres in whole nerve trunks traced through multiple consecutive internodes. *J Neurocytol* 23:555–564.